

Aerostructural Design of Drone Mermoz

(Final report)

Mario Izquierdo-Serra*, Greta Sala*, Nikola N. Gavrilović† and Nicolas Gourdain‡

*Institut Supérieur de l’Aéronautique et de l’Espace (ISAE-SUPAERO), Université de Toulouse, 31055 Toulouse, FRANCE

Email: mario.izquierdo-serra@student.isae-supaero.fr

greta.sala@student.isae-supaero.fr

†Institut Supérieur de l’Aéronautique et de l’Espace (ISAE-SUPAERO), Université de Toulouse, 31055 Toulouse, FRANCE

Email: nikola.gavrilovic@isae-supaero.fr

‡Institut Supérieur de l’Aéronautique et de l’Espace (ISAE-SUPAERO), Université de Toulouse, 31055 Toulouse, FRANCE

Email: nicolas.gourdain@isae-supaero.fr

Abstract—This paper examines “Drone for Earth”, a project by ISAE Supaero concerning the realization of a long-range unmanned aircraft system (UAS) powered by hydrogen fuel cells with the capability of crossing the Atlantic Ocean. The aim of this study is the aerostructural analysis and design of Drone Mermoz (the object of the “Drone for Earth” project) and the evaluation of its performance.

In the field of UAS, high range and endurance capabilities are often accomplished through medium-to-high aspect ratio wings. The core problem of this widely employed design is the high flexibility of the airframe, which affects the way a wing is deformed during flight and ultimately impacts the aerodynamic performance of the aircraft.

In an effort to achieve a realistic aero-structural analysis of the UAS, it is essential to take into account nonlinear aeroelasticity phenomena. For this reason, part of the study will be performed using AWSING, a software for the study of aircraft with flexible high aspect-ratio surfaces. Furthermore, this work aims to apply modifications on the design of the wing spar, seeking an optimization of the drone performance.

I. STUDY OF THE ART

As unmanned aircraft system applications are spreading within the military, civil and commercial fields, the demand for UAS capable of sustaining long flights is becoming pressing. This need, together with the motivation of reducing the environmental impact, has recently driven the development of electrical UAS [10].

Traditionally, the focus has always been on lithium-based batteries; however, their low energy density introduces a limit in terms of range and endurance, paving the way for other solutions such as hydrogen fuel cells to be incorporated on these aircraft. Hydrogen fuel cells have become more popular over the past years due to several advantages with respect to other energy sources [11]. Firstly, the power provided per flight hour is five times greater than that of lithium-based batteries (for the same weight). In addition, they offer a better reliability and require a lower level of maintenance than internal combustion engines.

In this context, the “Drone for Earth” concerns the conception of a light weight UAS that can cross the South Atlantic following the path mapped by Jean Mermoz from Dakar (Senegal) to Natal (Brazil) (route used by the French aviation company “Aéropostale” in the 1930s). Up to now, this journey

has only been completed using UAS with internal combustion engines. The goal of this project is to complete this flight with an electrical propulsive system and hydrogen fuel cells.

Drone Mermoz is conceived as a medium-to-high wing aspect ratio aircraft. This type of wing is appealing because it optimizes the lift-to-drag ratio as well as minimizing structural weight. Yet, the design results in a slender and very flexible airframe. Wing flexibility induces deformation and oscillation of the structure, thus provoking a non-negligible impact on aircraft performance. At its worst, wing flexibility leads to destructive fluid/structure interactions such as torsional divergence or flutter [8].

As a matter of fact, the design of an aircraft should always integrate aerodynamics, structural dynamics and control system laws, and an aim to resolve their conflicts. However, as aspect-ratios are increased nonlinear aeroelastic effects become more prevalent, significantly complicating the prediction of the structure’s behaviour [5]. This is the reason why a thorough aerostructural analysis is required for Drone Mermoz.

II. INITIAL DATA AND PROBLEM STATEMENT

The “Drone for Earth” project is based on three basic mission requirements:

- 1) Ability to cross a distance of 3000 km.
- 2) Total mass of less than 25 kg.
- 3) Hydrogen fuel cells as the primary energy source.

The main purpose of this work is to show the importance of the aerodynamic and structural coupling present in Drone Mermoz. In order to perform the analysis, a considerable amount of data concerning the drone’s most recent design were provided. In Tab. I and Tab. II a schematic geometric model of the drone and a mass breakdown of the main components is presented, respectively. They are not sufficient to implement an aerostructural analysis; nevertheless, they constitute a reference and represent the starting point for the development of this study. In Tab. I, L.E. stands for leading edge and T.E. for trailing edge, while the origin for longitudinal positions is located at drone’s nose. Additionally, a T-tail and a high wing configuration are present in Drone Mermoz. This layout is also a part of drone’s most recent design.

TABLE I
DRONE MERMOZ GEOMETRY

Wing		
Span (2b)	3.60	<i>m</i>
Root Chord	0.26	<i>m</i>
Root L.E. position	0.38	<i>m</i>
Root T.E. position	0.64	<i>m</i>
Root mid-section position	0.51	<i>m</i>
Tip Chord	0.10	<i>m</i>
Tip L.E. position	0.46	<i>m</i>
Tip T.E. position	0.56	<i>m</i>
Tip mid-section position	0.51	<i>m</i>
Surface	0.648	<i>m</i> ²
Mean Aerodynamic Chord	0.19	<i>m</i>
Twist	2.00	°
Airfoil	S7075	
Horizontal Tail		
Span (2b)	0.80	<i>m</i>
Root Chord	0.15	<i>m</i>
Root L.E. position	1.60	<i>m</i>
Root T.E. position	1.75	<i>m</i>
Root mid-section position	1.675	<i>m</i>
Tip Chord	0.08	<i>m</i>
Tip L.E. position	1.635	<i>m</i>
Tip T.E. position	1.715	<i>m</i>
Tip mid-section position	1.675	<i>m</i>
Surface	0.092	<i>m</i> ²
Airfoil	HT12	
Vertical Tail		
Span	0.20	<i>m</i>
Root Chord	0.18	<i>m</i>
Root L.E. position	1.50	<i>m</i>
Root T.E. position	1.68	<i>m</i>
Root mid-section position	1.59	<i>m</i>
Tip Chord	0.12	<i>m</i>
Tip L.E. position	1.60	<i>m</i>
Tip T.E. position	1.72	<i>m</i>
Tip mid-section position	1.66	<i>m</i>
Surface	0.06357	<i>m</i> ²
Airfoil	HT12	
Fuselage		
Total length	1.68	<i>m</i>
Max diameter	0.24	<i>m</i>

In addition, drone's cruise condition performance is provided as a reference, which will be useful for validating the results obtained in the forthcoming sections. Cruise reference data are presented in Tab. III, where V refers to cruise airspeed, h indicates the cruise altitude, L/D represents the lift-to-drag ratio and Cl and Cd denote the average lift and drag coefficients. These reference parameters derive from drone's most recent design.

A first geometry model of the UAS is introduced in ASWING [6] (Fig. 1). As mentioned in the previous section,

TABLE II
DRONE MERMOZ COMPONENT MASS BREAKDOWN

Component	Mass (Kg)	Component	Mass (Kg)
Propeller	0.22	Motor	0.35
Payload	0.80	Camera	0.30
Fuel Cell Module	0.93	Regulator	0.20
Heat Exchanger	0.10	Servos	0.3
Solar Cells	0.3	Autopilot	0.50
Tubes	0.09	Hydrogen	0.42
Reservoir	2.70	Battery	0.30
Total component mass		7.51 kg	
Structural mass		4.94 kg	
Total mass		12.45 kg	

TABLE III
REFERENCE CRUISE PERFORMANCE PARAMETERS

V (m/s)	23
h (m)	100
L/D	24.9
Cl	0.59
Cd	0.0237

ASWING is the program selected to perform the analysis, as it was conceived for the prediction of static and quasi-static loads and deformations of aircraft with flexible high aspect ratio surfaces and fuselage beams. ASWING uses a fully nonlinear Bernoulli-Euler beam representation for all the surface and fuselage structures, while an enhanced lifting-line representation is employed to model the aerodynamic surface characteristics. The lifting-line model employs wind-aligned trailing vorticity, a Prandtl-Glauert compressibility transformation [5].

In ASWING, the aircraft structure is defined as a set of lifting and non-lifting beams. Four beams are defined to describe the UAS in question: the fuselage, the wing and the horizontal and vertical tails (H-tail and V-tail). The section aerodynamic properties of the lifting beams (wing and tail surfaces) have to be entered into ASWING. Hence, this paper starts by examining the software requirements in terms of airfoil aerodynamic characteristics: lift slope, zero lift angle of attack, maximum and minimum lift coefficient, profile drag coefficient, skin friction drag coefficient, and moment coefficient at each surface section. Considering that ASWING is capable of linearly interpolating these coefficients between two adjacent sections and that all three lifting surfaces have a trapezoidal shape, only the airfoil at the root and tip sections will be analyzed.

XFOIL has been identified in previous studies to be an appropriate tool to estimate airfoil aerodynamic properties [7]. In this case, XFLR5 is the specific selected tool. This is an analysis tool for airfoils, wings and planes operating at low Reynolds Numbers, which includes XFOIL's direct and inverse analysis capabilities, based on the Lifting Line Theory, on the Vortex Lattice Method, and on a 3D Panel Method.

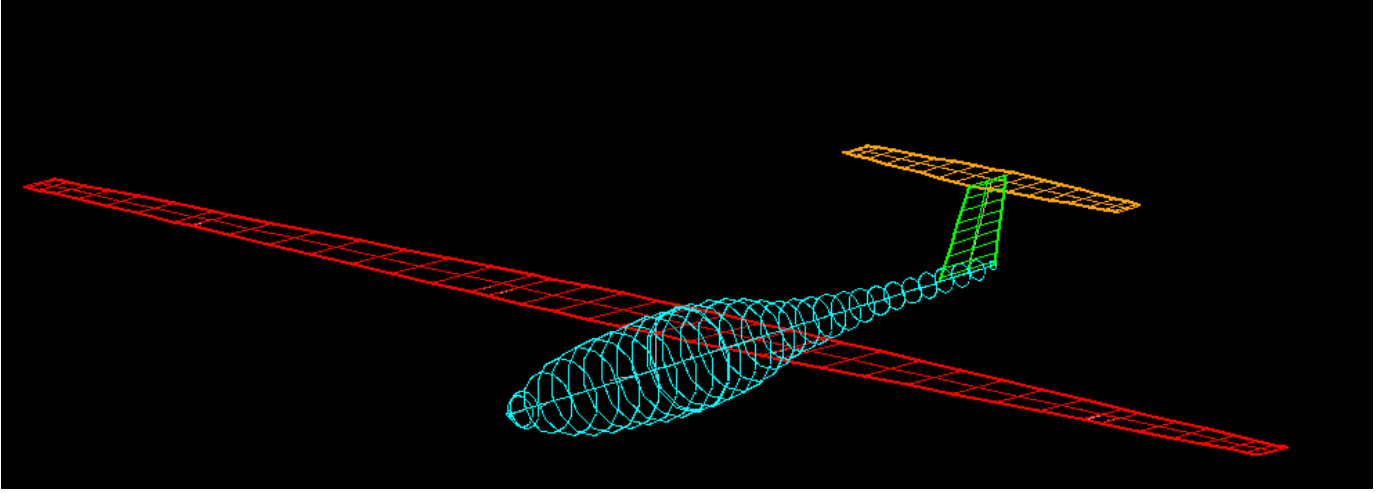


Fig. 1. Visual rendering of Drone Mermoz's initial model on ASWING

For the purposes of this study, ASWING outputs of interest are aircraft aerodynamic coefficients as function of the angle of attack, as well as aircraft deflections and aerodynamic forces and moments, which are estimated at different set-ups.

The next intended step of this study will be the aircraft mass estimation and the positioning of drone's main components in order to grant a stability margin of at least 10% of the mean aerodynamic chord. Furthermore, a discussion of structural component stiffness is one of the central scopes of this paper. Therefore, a section is dedicated to the evaluation of beam's stiffness according to De Saint-Venant beam theory.

The followed procedure will consist of simulating both a rigid and a flexible UAS model and comparing their performances and responses. A rigid model representation is possible, since an infinite value is assumed by ASWING when no input is made regarding the surface stiffness. Lastly, according to observed results, possible changes in the design will be proposed to optimize the aircraft in normal flight conditions [10].

III. AIRFOIL PERFORMANCE EVALUATION

As stated in the previous section, XFLR5 is the software selected for the estimation of the 2-D airfoil aerodynamic coefficients. For a cruise altitude of approximately $h = 100$ m and with an average speed of $V = 23$ m/s, the Reynolds number of each airfoil section is evaluated and inserted in XFLR5 as an input. The results obtained for the aerodynamic coefficients of interest are shown in Tab. IV and Tab. V. They serve as input data on ASWING to describe the airfoil properties and behaviour.

The aerodynamic coefficients of interest are: maximum and minimum lift coefficient (Cl_{max} and Cl_{min}), zero lift angle of attack (α_{zl}), profile drag coefficient (Cd_0), skin friction drag coefficient (Cd_{f0}), pressure friction drag coefficient (Cd_{p0}), moment coefficient (Cm_0) and lift slope (Cl_α).

In order to estimate aircraft's overall drag coefficient, the drag generated by the fuselage must be considered as well.

TABLE IV
WING AERODYNAMIC COEFFICIENTS

Airfoil	S7075	
Thickness	9%	
Section	Root	Tip
Reynolds	393,421	151,316
Cl_{max}	1.491	1.35
Cl_{min}	-0.41	-0.45
α_{zl} ($^\circ$)	-3.64	-2.17
Cd_0	0.015	0.01
Cd_{p0}	0.01	0.004
Cd_{f0}	0.005	0.006
Cm_0	-0.098	-0.07
Cl_α (rad^{-1})	6.8286	8.086

TABLE V
VERTICAL AND HORIZONTAL TAIL AERODYNAMIC COEFFICIENTS

Airfoil	HT12			
Thickness	5%			
Section	H-tail Root	H-tail Tip	V-tail Root	V-tail Tip
Reynolds	226,974	121,053	272,368	181,579
Cl_{max}	0.8	0.713	0.692	0.748
Cl_{min}	-0.74	-0.713	-0.692	-0.748
α_{zl} ($^\circ$)	0	0	0	0
Cd_0	0.006	0.0086	0.0058	0.007
Cd_{p0}	0.0014	0.0019	0.00127	0.00155
Cd_{f0}	0.0046	0.0067	0.00453	0.00545
Cm_0	0	0	0	0
Cl_α (rad^{-1})	6.4	6.4	6.4	6.4

Typical drag coefficient values for different shapes of fuselages are found in [3], where it was possible to find a value for Mermoz's fuselage Reynolds number and length-to-diameter ratio (l/D). Fuselage friction and pressure drag coefficients (Cd_f and Cd_p) are shown in Tab. VI.

Lastly, XFLR5 is also used to model the elevator on the horizontal tail. The presence of this control surface is fundamental for the sake of longitudinal equilibrium of an aircraft, which is the reason why ASWING requires the rate of change of lift and moment due to surface deflection ($Cl_{elevator}$ and $Cm_{elevator}$) in order to trim the aircraft. Through the use of this tool, it is possible to simulate the change of forces and moments on the tail section airfoils depending on the deflection of the elevator. The obtained results are collected in Tab. VII.

TABLE VI
FUSELAGE DRAG COEFFICIENTS

Reynolds	1, 111, 773
l/D	7.0
Cd_f	0.0101
Cd_p	0.4

TABLE VII
LIFT AND MOMENT SLOPE DUE TO ELEVATOR DEFLECTION

Airfoil	HT12	
Hinge position in chord	50%	
Section	H-tail Root	H-tail Tip
$Cl_{elevator}$ (rad^{-1})	0.330	0.327
$Cm_{elevator}$ (rad^{-1})	-0.0185	-0.0175

IV. STIFFNESS EVALUATION

One of the main objectives of this study is the comparison of the behavior of a rigid and a flexible Drone Mermoz model. The rigid model is equipped with a wing, a tail and a fuselage with extremely high torsional, extensional and bending stiffness. In ASWING, beam section stiffness can be defined for the aircraft structural components. When no input is introduced for these parameters, the program automatically considers infinite stiffness, i.e. a rigid model. Therefore, for the definition of a realistic flexible model, it is necessary to choose an appropriate method to calculate the rigidity of the sections of interest.

In order to study the aerostructural coupling of the drone, and for the definition of the flexible model, the beams of fundamental structural importance have to be selected. In this case, only the wing and the horizontal tail are considered since they present a greater deformation in flight. Therefore, the vertical tail and fuselage are considered as rigid also in the flexible model, in order to simplify the present work and focus on the important surfaces. Since the drone is defined as a set of beams in ASWING, the results of De Saint-Venant's beam theory can be used to calculate the rigidity of the wing and horizontal tail.

De Saint-Venants' theory applies to 3D bodies with the following characteristics:

- 1) The body is slender, that is, it has a much greater dimension in one direction with respect to the others.
- 2) The body is obtained by the rigid translation of the section, which is equal to itself along the beam axis.
- 3) The beam is homogeneous, isotropic, and elastic.
- 4) Loads and constraints are applied at the extreme section.

The wing structure can be studied under this model. Even though wing load is distributed and the wing is tapered, only section properties will be evaluated with this theory. Therefore, differences with respect to the selected model are small, justifying the choice. Both the wing and the horizontal tail are designed with a spar, placed at the airfoil's thickest point. The spar is the most important structural element of the whole wing-box. Generally, two types of load act on a wing (or semi-wing): those due to aerodynamic factors and those due to the weight of the wing itself. In particular, the two main loads due to aerodynamic factors are lift and torque. The lift is a force distributed over the entire wing and causes a bending moment. The structural element that bears this load is the spar [4]. Therefore, the bending stiffness of the wing (and the horizontal tail) is assimilated to that of the spar itself.

This assumption will lead to inaccurate results for the in-plane bending stiffness, since the spar is not the structural element in charge of sustaining the in-plane bending moment. However, the limitation of the model will not be relevant for the cruise performance evaluation, due to the small in-flight wing deformation in that direction.

Knowing that E is the Young modulus of the spar material, and that I_x and I_y are the moments of inertia of the spar section, bending stiffness (K_x and K_y) is evaluated as shown in (1) and (2).

$$K_x = E \cdot I_x. \quad (1)$$

$$K_y = E \cdot I_y. \quad (2)$$

The torsional rigidity of a wing is calculated using the closed section formed by the ensemble of the front spar (in this case, the only spar present) and the leading-edge skin. Therefore, the torsional stiffness of this model is evaluated using De Saint-Venants' solution for thin-walled closed sections. Furthermore, for simplicity, the thinned-walled section is approximated to a ring of constant thickness t . Considering that J is the polar moment of inertia of a section, G , the shear modulus, and ν , the Poisson's coefficient of the chosen material, the torsional stiffness (K_t) is evaluated as explained in (3) and (4).

$$G = \frac{E}{2 + 2\nu}. \quad (3)$$

$$K_t = G \cdot J. \quad (4)$$

Lastly, the extensional stiffness (K_e) of the section is evaluated as presented in (5), where A is the area of the spar

section under study. Once again, the extensional stiffness of the whole wing section is approximated to the spar stiffness.

$$K_e = E \cdot A. \quad (5)$$

For Drone Mermoz's initial design, a spar of circular section of diameter D (radius r) is chosen for both the wing and the horizontal tail, with an overall average thickness for the thin-walled section t . Each spar has a length L , which is equal to the surface semi-span. The graphic representation of this spar is portrayed in Fig. 2. The formulas for estimating the stiffness are shown in (6) and (7). Spar geometry and stiffness are presented in Tab. VIII.



Fig. 2. Representation of initial spar model of Drone Mermoz

$$J = \frac{\pi t D^3}{4}. \quad (6)$$

$$I_x, I_y = \frac{\pi r^4}{4}. \quad (7)$$

TABLE VIII
ROD SPAR GEOMETRY AND STIFFNESS

	Wing		H-Tail	
	Root	Tip	Root	Tip
E (MPa)	135000			
ν	0.18			
r (mm)	10.1	3.3	2.95	1.2
L (mm)	1800		400	
A (mm ²)	320.4739	34.2119	27.3397	4.5239
t (mm)	3		2	
I_x, I_y (mm ⁴)	8172.9	93.142	59.481	1.6286
J (mm ⁴)	1.01e6	5.7465e4	3.4114e4	5.1752e3
K_x, K_y (Nm ²)	1103.34	12.574	8.0299	0.2198
K_e (N)	4.3264e7	4.6186e6	3.6909e6	6.1073e5
K_t (Nm ²)	5.7776e4	3.2872e3	1.9514e3	2.96e2

V. MASS ESTIMATION

The following section comprises an estimation of Drone Mermoz's structural mass, which represents a key stage of its aerostructural design. This mass together with that of

the components yield the aircraft total mass. It is important to recall that, according to mission requirements, total mass should not exceed 25 kg. In addition, the weight/span ratio at each section has to be introduced in ASWING for each of the defined surfaces (wing, fuselage, horizontal and vertical tail).

Wing mass is computed taking into account two structural elements. On the one hand, the mass of the skin is calculated. In order to do so, two layers of carbon cloth at 0°/90° are employed as the base material. It should be remarked that the mentioned layers are placed all over the upper and lower wing surfaces. Two extra layers are placed in the vicinity of the root section and an additional one at the tip surrounding area. The purpose of these extra layers is that, as the span increases, the bending moment carried by the wing root requires reinforcement with additional material. Properties of the chosen carbon cloth are shown in Tab. IX. The mass of the skin is obtained by taking into account the wing surface, total average skin thickness and density of the chosen material.

TABLE IX
CARBON CLOTH LAYER CHARACTERISTICS

Density (kg/m ³)	1428.6
Thickness (mm)	0.4

On the other hand, the mass of the spars (one for each half-wing) is computed considering the selected geometry and material (unidirectional carbon fiber). The chosen material has a density of $\rho = 1544 \text{ kg/m}^3$.

Once the structural mass is calculated, it has to be distributed along the span. Mass/span ratio is only computed for root and tip sections, and then ASWING performs a linear interpolation between them. The total mass of the wing is divided into three different categories: skin mass (uniformly distributed along the surface), reinforcement mass and spar mass. Adding the contribution to the mass/span ratio of each category enables the values to be inserted into ASWING for the root and tip sections. These values are shown in Tab. X, where they refer to each half-wing (since left-right symmetry is applied).

Horizontal tail mass is computed following the same procedure as the wing, with the only difference that no extra carbon cloth layers are placed to reinforce the root section. This decision is taken due to the considerably smaller horizontal tail span, when compared to that of the wing. The material employed for the skin and the spar remains unchanged from that of the wing.

Considering the vertical tail, no spar or reinforcement is selected, so only skin mass is taken into account. The mass/span ratios of the whole vertical tail are shown in Tab. X (no left-right symmetry is applied).

Lastly, fuselage mass is entirely estimated through its skin mass. The material employed remains unchanged (2 carbon layers) and the only difficulty is related to the fuselage wetted surface calculation. In order to obtain the most precise result, the geometry has been divided into 4 different volumes, whose external surfaces are calculated and then added. Front volume

TABLE X
DRONE MERMOZ MASS/SPAN RATIOS

Surface	Mass/span (kg/m)	
	Root	Tip
Wing	1.4503	0.4583
H-tail	0.3663	0.2032
V-tail	0.8229	0.5486

is assimilated to a paraboloid, due to its particular shape. This first volume is followed by a cylinder and by a conical frustum. Finally, the rear part of the fuselage is calculated as a cone. By making use of those four divisions, a much closer representation of fuselage surface is obtained.

As a last step before computing the total structural mass, the miscellaneous mass has to be estimated. This mass represents connections, additional hinge material, construction errors, etc. It is calculated as a fixed percentage of the total wing mass. Taking $k_{miscellaneous} = 0.08$ gives good results when compared to previous composite parts [2]. In (8), the formula used to compute miscellaneous mass ($M_{miscellaneous}$) from wing mass (M_{wing}) is shown. Finally, in Tab. XI a summary of beam masses together with miscellaneous and total mass is presented.

$$M_{miscellaneous} = k_{miscellaneous} \cdot M_{wing} \quad (8)$$

TABLE XI
DRONE MERMOZ STRUCTURAL MASS

	Mass (kg)
Wing	3.4354
H-tail	0.2278
V-tail	0.1453
Fuselage	1.6155
Miscellaneous	0.2748
TOTAL	5.6990

Some conclusions can be drawn from Tab. XI. First of all, wing mass represents approximately 60% of total structural mass. Therefore, when seeking an optimization of drone performance, efforts should be made to reduce wing mass, since it is the element with the highest contribution. Fuselage and wing mass represent almost 90% of total mass, therefore, there is little interest on focusing on the tail for mass reduction.

The Drone Mermoz mass breakdown is shown in Tab. XII and its total mass is below the maximum specified in the requirements (25 kg). The structural mass fraction represents an important parameter, as it allows a comparison with other drones previously designed. In this initial design, the obtained percentage is slightly higher than in other drones (studies show that structure can be reduced to 40% of the total mass). This implies that there is still room for improvement in terms of structural mass design and computation. An optimization of the initial design will be proposed in the forthcoming sections to reduce the structural mass.

TABLE XII
DRONE MERMOZ MASS BREAKDOWN

Structural mass (kg)	5.699
Components mass (kg)	7.51
Total mass (kg)	13.209
Structural mass fraction	43.14%

VI. STABILITY MARGIN

Once the mass of each structural component has been calculated, it is now possible to place the aircraft components along the fuselage (or wing) to ensure longitudinal stability. A minimum static margin of 10% of the mean aerodynamic chord has to be respected.

The static margin allows the aircraft to be statically stable. It is the distance between the neutral point and the aircraft center of gravity (CG). The neutral point position, which is the hypothetical CG position where longitudinal stability is neutral, depends on the airfoils and on aircraft geometry. In this case, neutral point is located at $X_n = 0.54 m$, meaning that, to grant the required margin, the center of gravity must fall at $X_{cg} = 0.5215 m$ or forward.

Component positions for the initial design are decided based on their typical position on similar drones, but always ensuring the static margin. The exact location of each component is presented in Tab. XIII. It is necessary to point out, for the sake of clarity, that the solar panels and servo-commands are placed on the wings (at different span positions) and not on the fuselage, while the propeller is attached to the nose of the fuselage and all the other components are placed inside the fuselage. The hydrogen is placed inside the reservoir, which is the reason why they share the same X-position. A graphical representation of the components placement is shown in Fig.3. Dimensions of three important components (fuel cell module, reservoir and battery) have been taken into account to make sure all elements fit inside the fuselage.

TABLE XIII
DRONE MERMOZ COMPONENT POSITIONS

Component	X-position (m)	Component	X-position (m)
Propeller	0.0	Motor	0.035
Payload	0.06	Camera	0.10
Fuel Cell Module	0.23	Regulator	0.35
Heat Exchanger	0.42	Servos	0.44
Solar Cells	0.44	Autopilot	0.52
Tubes	0.64	Hydrogen	0.64
Reservoir	0.64	Battery	1.09
Center of gravity position		0.521 m	
Static Margin		10.25%	

VII. RIGID AND FLEXIBLE MODELS COMPARISON

The introduction of finite stiffness produces differences in the aircraft operation. For this reason, it is worth making a comparison between the two models. In this case, since the

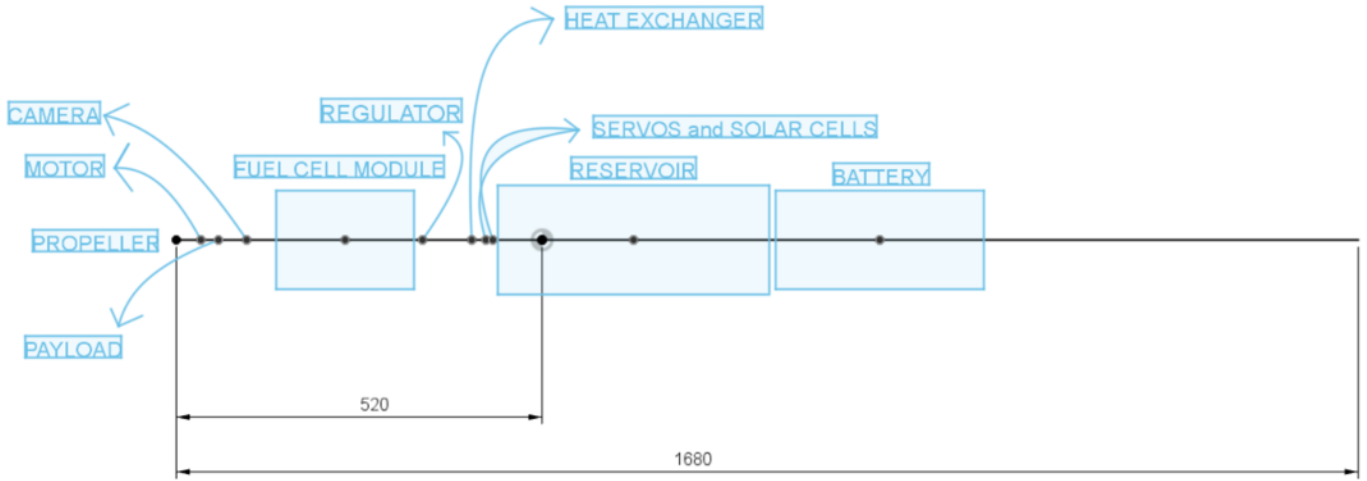


Fig. 3. Representation of component placement along Drone Mermoz's fuselage

lifting-line model employed by ASWING is not suitable for the prediction of the aircraft's lateral and directional dynamics, the focus will only be on the longitudinal aircraft behavior.

A. Longitudinal Stability

Firstly, longitudinal stability should be verified for both models. The verification can be done by checking that the sign of the lift moment coefficient slope is negative. Several simulations are performed on ASWING for both models at constant speed and altitude and for different angles of attack. ASWING will compute forces and moments at each angle of attack, from which it is possible to compute the lift coefficient (Cl) and lift moment coefficient (Cm) by means of (9) and (10).

$$Cl(\alpha) = \frac{2 \cdot L(\alpha)}{\rho \cdot V^2 \cdot S} \quad (9)$$

$$Cm(\alpha) = \frac{2 \cdot M(\alpha)}{\rho \cdot V^2 \cdot c \cdot S} \quad (10)$$

Where c is the mean aerodynamic chord of the aircraft, S is wing's surface, ρ is the air density at cruise altitude, V is the cruise airspeed, and L and M are the lift and the moment due to lift computed at a certain angle of attack, α . From the obtained coefficients, the lift coefficient slope (Cl_α) and moment coefficient slope (Cm_α) are computed. Results from rigid model are shown in Tab. XIV, while those of the flexible model are presented in Tab. XV. Finally, a comparison between both models is made in Tab. XVI.

It can be noted that Cm_α is negative in both cases. Therefore, the two models are longitudinally statically stable. The observed differences between the average slope coefficients are so small that are neglected.

B. Cruise Condition Parameters

The two models are simulated on ASWING in order to obtain cruise condition performance parameters. Altitude ($h = 100$ m) and cruise velocity ($V = 23$ m/s) remain unchanged

TABLE XIV
RIGID AIRCRAFT COEFFICIENTS

Rigid Aircraft				
α ($^\circ$)	Cl	Cm	Cl_α (rad^{-1})	Cm_α (rad^{-1})
-10	-0.452	1.411	4.7087	-12.43
-6	-0.181	0.704	6.913	-18.56
-2	0.306	-0.623	7.013	-19.27
0	0.551	-1.308	7.015	-19.42
2	0.794	-1.999	6.998	-19.54
6	1.253	-3.331	6.837	-19.36
10	1.45	-4.034	5.729	-16.801
14	1.527	-4.354	4.729	-14.159
18	1.568	-4.504	3.992	-12.02
Average Cl_α (rad^{-1})			5.9923199	
Average Cm_α (rad^{-1})			-16.8433059	

TABLE XV
FLEXIBLE AIRCRAFT COEFFICIENTS

Flexible Aircraft				
α ($^\circ$)	Cl	Cm	Cl_α (rad^{-1})	Cm_α (rad^{-1})
-10	-0.452	1.412	4.7086	-12.43
-6	-0.181	0.704	6.913	-18.56
-2	0.306	-0.623	7.013	-19.27
0	0.551	-1.308	7.015	-19.42
2	0.794	-1.999	6.998	-19.54
6	1.253	-3.329	6.837	-19.35
10	1.44	-4.029	5.725	-16.78
14	1.526	-4.348	4.726	-14.14
18	1.567	-4.496	3.990	-12.00
Average Cl_α (rad^{-1})			5.992133	
Average Cm_α (rad^{-1})			-16.836727	

TABLE XVI
COEFFICIENTS COMPARISON

Coefficient	Rigid Model	Flexible Model	Percent. Change
Cl_α (rad^{-1})	5.993199	5.9921331	0.02%
Cm_α (rad^{-1})	-16.8433959	-16.83672	0.04%

for the two models. Simulation results are shown in Tab.XVII, where Cl and Cd are the average lift and drag coefficients, the cruise angle of attack is α , and $\alpha_{elevator}$ is the elevator's deflection angle required to trim the aircraft in cruise conditions.

TABLE XVII
CRUISE PERFORMANCE PARAMETERS

	Rigid	Flexible
L/D	25.36	25.34
Cl	0.5889	0.588
Cd	0.02322	0.0232
α ($^\circ$)	0.05	0.04
$\alpha_{elevator}$ ($^\circ$)	0.94	0.94

Recalling the initial reference data described in section II, it can be noted that the aircraft cruise performance values obtained in ASWING are close to the reference design values provided. These results confirm the validity of the models developed in this work so far.

C. Comparison between the Models

The similarity of the two models is due to the high stiffness of the chosen rod spar for the initial design. When the lifting surface tip undergoes a vertical displacements due to bending moment, the angle of attack is varied, affecting the lift coefficient. In this case, it can be noted that, at high angles of attack, the performance of the flexible aircraft is slightly decreased (Tab. XVI), possibly indicating an anticipated stall phenomenon. In addition, the distribution of aerodynamic loads on a surface can produce a non-zero elastic twist distribution in the surface, increasing or diminishing the effective angle of attack. However, as mentioned above, the initial model is so stiff that it does not allow the observation of such effects. Nevertheless, other spar geometries and sizes, which may present a smaller stiffness, can be endorsed for this study.

VIII. OPTIMIZATION STRATEGY : I-SHAPED SPAR

A. Structural Properties of the I-Shaped Spar

As discussed in the *Stiffness Evaluation* paragraph, the initial wing model included a spar with a circular section. This model was selected because of its practical shape and due to the lower manufacturing cost when compared to other shapes. Eventually, this choice resulted in a remarkably stiff and heavy wing. By exploiting a more efficient spar section shape, as an I-shaped section, it is possible to achieve satisfactory stiffness values and an overall lighter wing.

The elements that contribute to the construction of the spar are: the vertical web, which resists shear forces, and a pair

of flanges, which absorb the bending moment, by means of tensile and compression forces (Fig. 4). Nevertheless, this spar model presents some inconveniences such as a higher complexity and cost of the manufacturing process. In fact, due to the reduced size of the horizontal tail airfoil section, an I-shaped spar that fits inside its wing-box will be almost impossible to produce with regular-sized technologies. For this reason, a redesign of the wing spar is done, while keeping a circular section spar in the horizontal tail. An I-section is the selected spar section for the wing (Fig. 5).



Fig. 4. Representation of the I-shaped spar of Drone Mermoz's wing

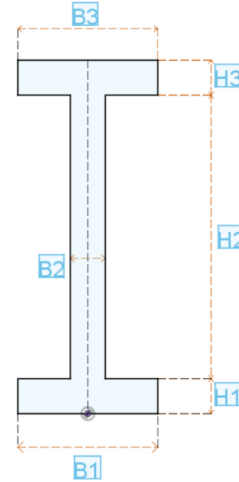


Fig. 5. Representation of the I-shape spar section of Drone Mermoz's wing

The calculation of the torsional stiffness is still performed following the aforementioned procedure. However, different formulas are used for the computation of the moments of inertia of an I-shaped section. First of all, in (11) and (12), the moments of inertia of each of the three rectangular sections are calculated ($I_{x,i}$ and $I_{y,i}$). Then, the I-shaped moments of inertia (I_x and I_y) are computed according to (13) and (14), where $d_{y,i}$ and $d_{x,i}$ are the vertical and horizontal distances between each rectangle's centroid and the overall section's centroid. New stiffness values for the wing's sections of interest are shown in Tab. XVIII.

$$I_{x,i} = \frac{b_i h_i^3}{12} \quad (11)$$

$$I_{y,i} = \frac{h_i b_i^3}{12} \quad (12)$$

$$I_x = \sum_{i=1}^3 (I_{x,i} + A_i d_{y,i}^2). \quad (13)$$

$$I_y = \sum_{i=1}^3 (I_{y,i} + A_i d_{x,i}^2). \quad (14)$$

TABLE XVIII
I-SHAPED SPAR GEOMETRY AND STIFFNESS

	Wing Root		Wing Tip	
E (MPa)	135000			
ν	0.18			
	H (mm)	B (mm)	H (mm)	B (mm)
Rectangle 1	2	8	1	5
Rectangle 2	16.2	2	4.6	2
Rectangle 3	2	8	1	5
L (mm)	1800			
A (mm ²)	64.4		19.2	
t (mm)	1		2	
J (mm ⁴)	3.3667e5		3.831e4	
I_x (mm ⁴)	3369.2		95.456	
I_y (mm ⁴)	181.5		23.9	
K_x (Nm ²)	454.84		12.887	
K_y (Nm ²)	24.498		3.2265	
K_e (N)	8.694e6		2.592e6	
K_t (Nm ²)	1.9259e4		2.19e3	

As stated at the beginning of this section, the main expected advantage of the I-Shaped spar is the weight saving. The mass of the new spar and the percentage mass change are presented in Tab. XIX. Before proceeding, it should be pointed out that, since the wing mass has changed from the initial model, the CG is also affected. Therefore, aircraft components have to be relocated inside the fuselage to grant the minimal static margin required. By modifying the battery's position, the static margin is guaranteed. The battery is now located at $x = 1.03$ m, what represents a displacement of 5.5% with respect to the original position. In other words, the design of the aircraft does not need any other major changes due to the replacement of the spar.

TABLE XIX
WEIGHT SAVINGS DUE TO I-SHAPED SPAR

	Rod Spar	I-Section Spar	% Change
Spar mass (kg)	0.4217	0.11	74%
Wing mass (kg)	3.4354	2.812	18%
Structural mass (kg)	5.699	5.0257	12%
Drone mass (kg)	13.209	12.536	5%
Struct. mass fraction	43%	40%	3%

Finally, a closer look has to be taken at the results obtained after the optimisation process (Tab. XIX). Considerable savings are produced on the spar, the wing and the structural mass. However, the most remarkable results are those related to drone's total mass and structural mass fraction. On the one

hand, drone's total mass is reduced by 5%, which represents a great percentage since only the wing spar has been modified. On the other hand, with the I-shaped spar, the structural mass fraction is 40%. As mentioned above, similar drones, which have been previously designed and optimized, have a structure which represents 40% of the total mass. Those two results show that the weight optimization strategy was successful. The effect of the higher wing flexibility (due to redesigned spar) on drone's performance remains to be studied in further sections.

B. Longitudinal Stability and Cruise Condition

Following section VII, the new drone model equipped with an I-Section spar in its wing is simulated in ASWING in order to obtain longitudinal coefficients (Tab. XX and Tab. XXIII) and cruise condition performance (Tab. XXII).

TABLE XX
FLEXIBLE AIRCRAFT COEFFICIENTS

Flexible Aircraft (I-Shaped Spar)				
α (°)	C_l	C_m	$C_{l\alpha}$ (rad ⁻¹)	$C_{m\alpha}$ (rad ⁻¹)
-10	-0.453	1.365	4.719	-12.00
-6	-0.180	0.707	6.875	-18.869
-2	0.305	-0.646	6.990	-19.687
0	0.550	-1.313	7.003	-19.430
2	0.802	-1.909	7.069	-18.705
6	1.223	-2.455	6.674	-14.559
10	1.331	-2.534	5.145	-10.855
14	1.361	-2.609	4.122	-8.740
18	1.567	-2.638	3.466	-7.260
Average $C_{l\alpha}$ (rad⁻¹)			5.785	
Average $C_{m\alpha}$ (rad⁻¹)			-14.456	

TABLE XXI
COEFFICIENTS COMPARISON

Coefficient	Rigid Model	Flexible Model	Percent. Change
$C_{l\alpha}$ (rad ⁻¹)	5.993199	5.785	3.48%
$C_{m\alpha}$ (rad ⁻¹)	-16.8433959	-14.456	14.17%

TABLE XXII
CRUISE PERFORMANCE PARAMETERS

	Rigid	Flexible
L/D	25.34	25.33
C_l	0.5878	0.5878
C_d	0.0232	0.0232
α (°)	0.036	0.045
$\alpha_{elevator}$ (°)	0.9404	0.9227

From the obtained results, it can be noted that wing flexibility effects on the longitudinal coefficients, described in section VII, are now more visible. The observable changes are mainly due to the higher flexibility of the designed I-shaped spar when compared to the initial rod spar.

IX. FLEXIBILITY EFFECT ON THERMALS AND SINUSOIDAL GUST ENCOUNTERS

UAVs endurance performance can be hugely improved without the need of additional energy storage and weight. In recent years, there has been a considerable interest on extracting energy from the environment by actively searching out and taking advantage of thermals. Thermals are localized, warmer regions in the atmosphere moving upwards. They are created by the uneven heating of Earth's surface from solar radiation and they are an example of atmospheric convection [1]. Thermals are exploited by UAVs and gliders for soaring and gaining altitude. In general, it is convenient to gain as much altitude as possible by taking advantage of thermals. This will spare the overall thrust demand and consequently reducing aircraft fuel consumption. Therefore, by designing an aircraft so that it gains a higher altitude when encountering a thermal, its endurance performance can be improved.

Several works on the potential of wing flexibility in the exploitation of thermals have been carried out [12] [9], proving that wings with higher out-of-plane flexibility (flapping) cause higher altitude gains when a gust is encountered. The phenomenon can be explained by comparing the wing to a spring that stores energy. The bending of the structure delays lift augmentation when the gust is encountered. This in turn delays the weathercock effect, which diminishes the increased angle of attack caused by the upward gust. The energy stored in the wing will begin to lift the fuselage, but this occurs once the gust speed is already diminished. Therefore, when designing this type of drone, it is preferable to opt for wings with lower flapping stiffness. Among the two spar models proposed in this report, the I-spar is the one that presents less flapping stiffness, which is another reason why the I-shaped spar design will potentially represent a better design choice.

To study this phenomenon, the encounter of a thermal is simulated in ASWING. The thermal in question has a maximum upward velocity of 2 m/s and a maximum radius of 15 m. The radius has been chosen to be sufficiently big, so that the difference in vertical wind speed seen by the different parts of the aircraft is negligible. The drone flies through the center of the thermal as portrayed in Fig. 6, without changing the trimmed aircraft elevator deflection of cruise condition (fixed stick configuration). Three different flexible wings have been simulated, each one of them with an associated tip deflection.

After simulating the different models, tip deflections and gains in altitude are shown in Tab. XXIII. The results show that the encounter of a thermal increases the flight altitude. Yet, in contradiction to former findings, obtained values do not show that a higher flapping flexibility (higher tip deflection) causes greater altitude gains. It is plausible that limitations regarding the number of tested spars and gust types may have influenced the obtained results.

Another simulation is performed to model a sinusoidal upward gust. The gust modelled has a maximum upward velocity of 2 m/s and the sine wave has a length of 50 m, as it can be seen in Fig. 6. The results obtained in this simulation

TABLE XXIII
EFFECT OF FLEXIBILITY ON THERMAL ENCOUNTER

Model	Tip deflection (cm)	Height gain (m)
1	2.47	2.246
2	6.24	2.189
3	11.41	2.112

are presented in Tab. XXIV. Once again, the encounter of a gust increases the flight altitude, but the results do not show the expected trend on altitude gains.

TABLE XXIV
EFFECT OF FLEXIBILITY ON SINUSOIDAL GUST ENCOUNTER

Model	Tip deflection (cm)	Height gain (m)
1	2.47	4.931
2	6.24	4.835
3	11.41	4.707

As stated previously, the unsatisfactory results obtained from this limited analysis should be treated with considerable caution. The expected behavior has not been obtained, what does not mean that the theoretical study or the simulations are erroneous. A much deeper study should be carried out in order to fully understand this phenomenon. However, it is not in the purpose of this paper to further investigate the encounter of gusts.

X. CONCLUSIONS

The present study has developed an effective aerostructural design of Drone Mermoz. Starting from its geometric data, the goal was to achieve a given cruise aerodynamic performance and a reference structural mass estimation.

The first part of the work was dedicated to the design of a structural model equipped with a thick rod-like spar on the wing and the horizontal tail. The stiffness of the model were estimated following De Saint-Venant's theory and a conservative evaluation of the structural mass was obtained (5.66 kg). This resulted in, approximately, a 15% heavier structure than the reference one (4.94 kg). The aircraft performance in cruise conditions was then evaluated for the initial flexible model and a hypothetical rigid aircraft, both giving very close results to the reference ones ($L/D = 24.9$). The obtained lift-to-drag ratios for the flexible and rigid models were, respectively, 25.34 and 25.36.

In the second part of the study, the adoption of a more efficient spar section was proposed with the aim of reducing total structural weight. For this reason, an I-shaped section spar was selected for the wing. With the new spar, a total structural mass of 5.03 kg was achieved, which is only 1.8% greater than the expected one. The results also suggested that the use of an I-shaped spar would cause a more flexible wing. However, it is still possible to achieve good performance with an almost negligible lift-to-drag ratio loss.

Lastly, the altitude gain due to the encounter of thermals was investigated. In previous studies, it has been proven that

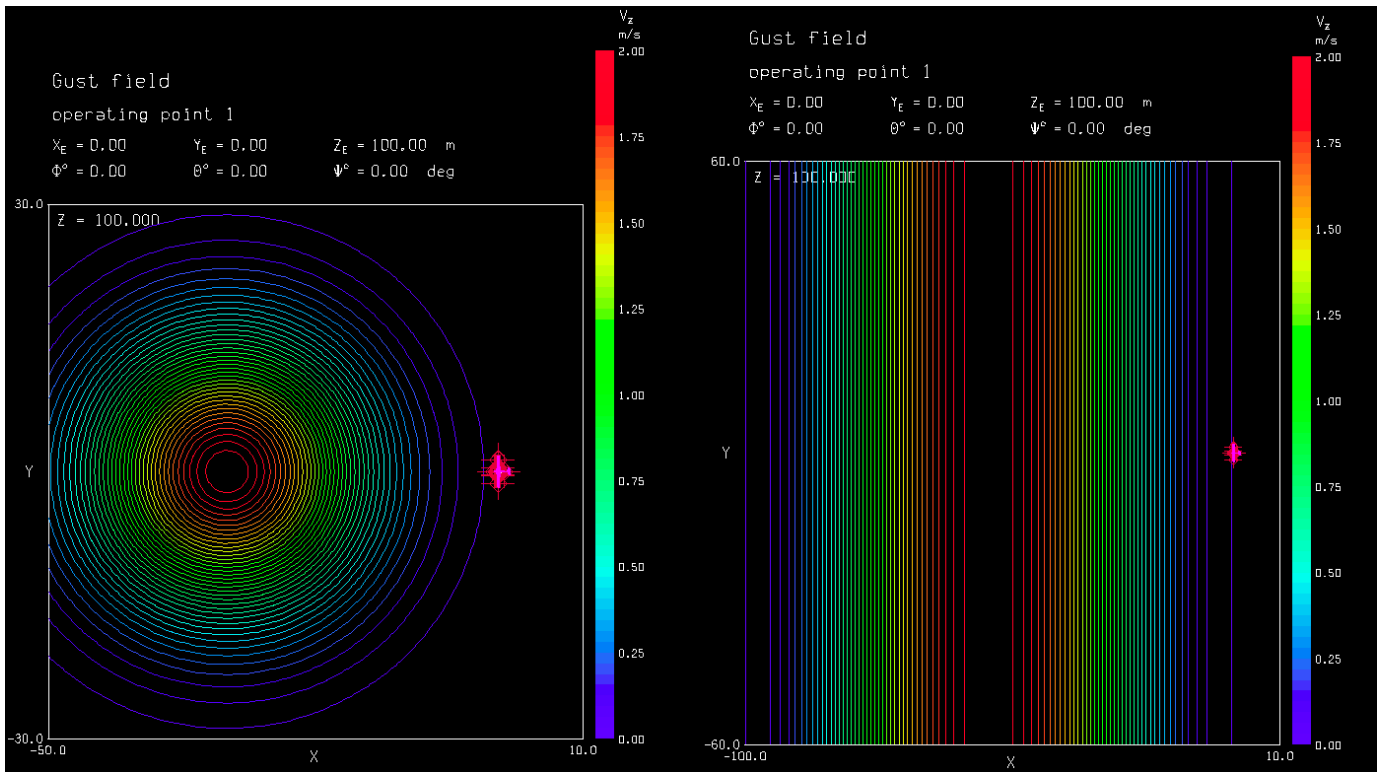


Fig. 6. Representation of thermal (left) and sinusoidal gust (right) encounter

high flexibility wings are more efficient when encountering gusts than more rigid wings. Nevertheless, the present study has not been successful in demonstrating such effect.

In conclusion, both models presented in this report comply with problem objectives and represent a valid aerostructural design for Drone Mermoz. However, selecting the I-shaped spar model will be more beneficial in the longer term. Manufacturing cost will be greater, but the I-shaped model presents a lower weight, hence less fuel request, and potentially allows a greater altitude gain in the occurrence of a thermal encounter.

ACKNOWLEDGMENT

The authors would like to thank Nikola N. Gravičević, for his help and advice throughout the development of this project, and Mark Drela, for his technical assistance with ASWING when it was requested.

REFERENCES

- [1] Tom Bradbury. *Meteorology and flight: Pilot's guide to weather (flying gliding)*. 2000.
- [2] Murat Bronz. *A contribution to the design of long endurance mini unmanned aerial vehicles*. PhD thesis, 2012.
- [3] Bruce Carmichael. *Minimizing fuselages' drag*. Fisher Flying Products, 1996.
- [4] Leone Corradi Dell'Acqua. *Meccanica delle strutture*. vol.1. McGraw-Hill, 2017.
- [5] Mark Drela. Integrated simulation model for preliminary aerodynamic, structural, and control-law design of aircraft. In *40th Structures, Structural Dynamics, and Materials Conference and Exhibit*, page 1394, 1999.
- [6] Mark Drela. *Aswing 5.99 technical description—steady formulation*. 2015.

- [7] Oscar Gonzales. *Static-stability analysis of a unmanned airplane as a flexible-body*. 2010.
- [8] Bertrand Kirsch, Olivier Montagnier, Emmanuel Bénard, and Thierry Faure. *Computation of very flexible high-aspect-ratio composite wing flutter speed using optimised open source solver*. 2018.
- [9] H Mai. *The effect of aeroelasticity upon energy retrieval of a sailplane penetrating a gust*. *OSTIV Publications*, 18, 1985.
- [10] Taylor McDonnell. *Multidisciplinary design optimization of flexible solar-regenerative high-altitude long-endurance aircraft*. 2018.
- [11] Karen Swider-Lyons, Richard Stroman, Gregory Page, and Joseph Rodgers. *Hydrogen fuel cell propulsion for long endurance small uavs*. page 6975, 2011.
- [12] Zsuzsa Ákos, Máté Nagy, Severin Leven, and Tamás Vicsek. *Thermal soaring flight of birds and unmanned aerial vehicles*. 2010.